Inorg. Chem. **2007**, *46*, 2388–2397

Inorganic Chemistry

Article

A Density Functional Study of the Electronic Structure and Spin Hamiltonian Parameters of Mononuclear Thiomolybdenyl Complexes

Simon C. Drew,*,†,‡ Charles G. Young,§ and Graeme R. Hanson*,†,‡

Centres for Magnetic Resonance and Metals in Biology, University of Queensland, Queensland 4072, Australia, and School of Chemistry, University of Melbourne, Victoria 3010, Australia

Received April 6, 2006

The electron paramagnetic resonance spin Hamiltonian parameters of mononuclear thiomolybdenyl complexes based upon the tris(pyrazolyl)borate ligand, together with their molybdenyl analogues, are calculated using density functional theory. The electronic **g** matrix and ^{95}Mo hyperfine matrix are calculated as second-order response properties from the coupled-perturbed Kohn–Sham equations. The scalar relativistic zero-order regular approximation (ZORA) is used with an all-electron basis and an accurate mean-field spin–orbit operator which includes all one- and two-electron terms. The principal values and relative orientations of the **g** and **A** interaction matrices obtained from the experimental spectra in a previous EPR study are compared with those obtained from unrestricted Kohn–Sham calculations at the BP86 and B3LYP level, and the latter are found to be in good quantitative agreement. A quasi-restricted approach is used to analyze the influence of the various molecular orbitals on **g** and **A**. In all complexes the ground state magnetic orbital is $d_{X^2-Y^2}$-based and the orientation of the **A** matrix is directly related to the orientation of this orbital. The largest single contribution to the orientation of the **g** matrix arises from the spin–orbit coupling of the d_{YZ}-based lowest-unoccupied molecular orbital into the ground state. A number of smaller, cumulative charge-transfer contributions augment the d–d contributions. A comparison of the theoretical EPR parameters obtained using both crystallographic and gas-phase geometry-optimized structures of Tp*MoO(bdt) (Tp* = hydrotris(3,5-dimethylpyrazol-1-yl)borate, bdt = 1,2-benzenedithiolate) suggests a correspondence between the metal–dithiolate fold angle and the angle of noncoincidence between **g** and **A**.

Introduction

In recent years, there has been a rapid growth in the implementation of quantum chemical calculations to calculate spectroscopic properties of metalloproteins and model compounds from first principles.[1] The prediction of phenomenological spin Hamiltonian (SH) parameters in electron paramagnetic resonance (EPR) from fundamental theoretical principles has been a challenge to theoreticians for half a century.[2] The computational speed of density functional theory (DFT) has enabled moderately large molecular structures to be modeled with the efficiency of Hartree–Fock methods and an accuracy comparable to low-level ab initio wave-function-based techniques. There have been many advances made in the application of DFT to the calculation of EPR parameters.[2] However, until very recently,[3] it has not been possible to properly treat relativistic effects of heavy-element complexes at the all-electron level and at one consistent level of theory.

In an earlier spectroscopic and structural study, we examined a class of model complexes based upon the thiomolybdenyl functional unit $[Mo^{V}{\equiv}S]^{3+}$ and the tris(pyrazolyl)borate ligand using EPR spectroscopy and compared the results with those obtained for some molybdenyl $[Mo^{V}{\equiv}O]^{3+}$ analogues.[4] Here we compute the SH parameters for the Tp*MoEX$_2$ series of complexes [E = O, S; Tp* = hydrotris(3,5-dimethylpyrazol-1-yl)borate; X = 2-(ethylthio)phenolate (etp), 2-propylphenolate (pp); X$_2$ = 1,2-benzenedithiolate (bdt), catecholate (cat)] from theory and compare

* To whom correspondence should be addressed. E-mail: sdrew@unimelb.edu.au (S.C.D.), graeme.hanson@cmr.uq.edu.au (G.R.H.).
† Centre for Magnetic Resonance, University of Queensland.
‡ Centre for Metals in Biology, University of Queensland.
§ School of Chemistry, University of Melbourne.

(1) Neese, F. *Curr. Opin. Chem. Biol.* **2003**, *7*, 125.
(2) Kaupp, M., Bühl, M., Malkin, V.G., Eds. *Calculation of NMR and EPR Parameters, Theory and Applications*; Wiley-VCH: Weinheim, Germany, 2004.
(3) Cosper, M. M.; Neese, F.; Astashkin, A. V.; Carducci, M. D.; Raitsimring, A. M.; Enemark, J. H. *Inorg. Chem.* **2005**, *44*, 1290.
(4) Drew, S. C.; Hill, J. P.; Lane, I.; Hanson, G. R.; Gable, R. W.; Young, C. G. *Inorg. Chem.* **2007**, *46*, 2373.

10.1021/ic060586b CCC: $37.00

Published on Web 02/17/2007

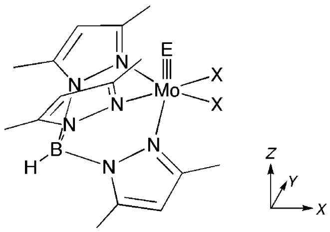

Figure 1. Structure of Tp*MoEX$_2$ (E = O, S; X = etp, pp; X$_2$ = bdt, cat). The molecular symmetry axes are labeled (*X*, *Y*, *Z*), with the *Z* axis directed along the Mo≡E bond and the *X* axis defined to bisect the equatorial X ligating atoms. Lowercase *x*, *y*, *z* and *x*′, *y*′, *z*′ are used to designate the principal axes of **g** and **A**, respectively.

them with previous experimental data, to understand the origin of the noncoincidence angles and the observed trends in the spin Hamiltonian parameters.

Theoretical Calculations

Single point calculations were carried out on an SGI Altix Bx2 (64 Itanium 2 CPUs and 121GB memory) at the high-performance computing unit at the University of Queensland using the ORCA program.[5] The full 58-atom X$_2$ = cat, bdt structures and the 84-atom X = etp and 88-atom X = pp structures of the Tp*MoEX$_2$ (E = O, S) series of complexes obtained from X-ray crystallography were used. The structures (Tables S11−S15, Supporting Information) for Tp*MoO(etp)$_2$, Tp*MoS(etp)$_2$, Tp*MoS(pp)$_2$, Tp*MoS(cat), and Tp*MoS(bdt) were taken from a previous spectroscopic and structural study.[4,6] The structure for Tp*MoO(cat) (Table S16, Supporting Information) was obtained from that of Tp*MoO(catCl$_4$)[7] by replacing the C−Cl bonds on the catecholate ring with shorter C−H bonds, and the structure of Tp*MoO(bdt) was taken from Dhawan and Enemark.[8] The crystallographic structure of Tp*MoO(pp)$_2$ was not available, and consequently, no DFT calculations were performed for this complex. Molecular axes were defined such that *Z* was parallel to the Mo≡E bond and *X* bisected the equatorial X ligating atoms (Figure 1). For the ideally C_s-symmetric bidentate complexes, the *Y* axis is therefore directed normal to the mirror (*XZ*) plane.

The interactions characterizing the properties of interest in this study are described by a phenomenological spin Hamiltonian (SH) of the form

$$H = \beta_e \sum_{\mu,\nu} g_{\mu\nu} B_\mu S_\nu + \sum_{\mu,\nu} A_{\mu\nu} S_\mu I_\nu \qquad (1)$$

where $\mu, \nu \in \{X, Y, Z\}$, **S** and **I** are the electron and nuclear vector spin operators, **g** and **A** are the 3 × 3 electron Zeeman and nuclear hyperfine coupling matrices, respectively, β_e is the Bohr magneton, and **B** is the applied magnetic field. The components of the ^{95}Mo hyperfine coupling (HFC) can be separated into various terms:[9−11]

$$A_{\mu\nu} = \delta_{\mu\nu} A_F + A_{\mu\nu}{}^{dip} + A_{\mu\nu}{}^{SO} \qquad (2)$$

Here the first term is the isotropic Fermi contact contribution (A_F), the second term the traceless first-order anisotropic spin-dipolar contribution (A^{dip}), and the third term is the nontraceless second-order contribution (A^{SO}), which incorporates spin−orbit coupling (SOC) of excited states into the singly (highest) occupied molecular orbital (S(H)OMO). The last term is commonly separated into the sum of an isotropic pseudocontact interaction and a second-order anisotropic contribution. The **g** matrix is obtained from the sum of a number of anisotropic shifts from the free electron *g* value, the most important being the second-order cross-term between the orbital Zeeman (OZ) and SOC operators

$$g_{\mu\nu} = \delta_{\mu\nu} g_e + \Delta g_{\mu\nu}{}^{RMC} + \Delta g_{\mu\nu}{}^{GC} + \Delta g_{\mu\nu}{}^{OZ/SOC} \qquad (3)$$

the other small first-order terms being the relativistic mass correction (RMC) and a diamagnetic gauge correction (GC).[2]

The spin-unrestricted Kohn−Sham equations were solved self-consistently and tightly converged using (i) the BP86 GGA functional incorporating Becke 88 exchange[12] and the Perdew 86 correlation[13] and (ii) the B3LYP hybrid functional incorporating Becke 88 exchange and Lee−Yang−Parr gradient-corrected correlation[14] and the 3 empirical parameters of Becke.[15] Scalar relativistic effects were treated at the all-electron level using the zeroth-order regular approximation (ZORA)[16] using the model potential implementation of van Wüllen,[17] in conjunction with a polarized triple ζ (TZVP) basis for Mo,[18] a TZVP basis for all N, S, and O atoms[19] and a SV(P) basis[20] on all C, H, and B atoms. The BP86 calculations employed the split-RI-J Coulomb approximation implemented in ORCA[5] using a suitable TZVP auxiliary basis.[21] To add flexibility to the core of the Mo atom, all bases were fully decontracted and the integration accuracy increased,[22] which ensured an accurate electron density at the Mo nucleus and hence a sensible prediction of the isotropic ^{95}Mo hyperfine coupling. An accurate mean-field method was used to account for the one- and two-electron (spin-own−orbit and spin-other−orbit) contributions to the Breit−Pauli spin−orbit coupling operator.[23] Using this effective SOC operator, the coupled-perturbed self-consistent field (CP-SCF) formalism was used to calculate both the **g** matrix (using the center of electronic charge as the gauge-dependent origin) and the ^{95}Mo **A** matrix at one consistent level

(5) Neese, F. *ORCA An ab initio, DFT and Semiempirical Electronic Structure Package*, version 2.4, revision 26; Max-Planck Institut für Bioanorganische Chemie: Mülheim, Germany, 2004.

(6) For Tp*MoO(etp)$_2$ the ethyl group attached to S(4) and for Tp*MoS(pp)$_2$ the propyl group attached to C(42) were found to be disordered. We arbitrarily used a single conformation of these complexes, with the expectation that disorder of this group is of little consequence to the SH parameters in comparison with the orientation of the six-membered ring to which it is attached. The structure of Tp*MoS(bdt) showed evidence of minor disorder. We used the structure with the occupancy factor of 0.975. The structure of Tp*MoS(cat) was also found to be disordered, and once again, we used the structure of the major component with occupancy factor 0.517. Hydrogen atoms for this complex were also added at standard bond angles and lengths.

(7) Basu, P.; Bruck, M. A.; Li, Z.; Dhawan, I. K.; Enemark, J. H. *Inorg. Chem.* **1995**, *34*, 405.
(8) Dhawan, I. K.; Enemark, J. H. *Inorg. Chem.* **1996**, *35*, 4873.
(9) Keijzers, C. P.; de Boer, E. *J. Chem. Phys.* **1972**, *57*, 1277.
(10) Belanzoni, P.; Baerends, E. J.; van Asselt, S.; Langewen, P. B. *J. Phys. Chem.* **1995**, *99*, 13094.
(11) Neese, F. *J. Chem. Phys. A* **2001**, *105*, 4290.
(12) Becke, A. D. *Phys. Rev. A* **1988**, *38*, 3098.
(13) Perdew, J. P. *Phys. Rev. B* **1986**, *33*, 8822.
(14) Lee, C.; Yang, W.; Parr, R. G. *Phys. Rev. B* **1988**, *37*, 785.
(15) Becke, A. D. *J. Chem. Phys.* **1993**, *98*, 5648.
(16) van Lenthe, E.; Baerends, E. J.; Snijders, J. G. *J. Chem. Phys.* **1993**, *99*, 4597. van Lenthe, E.; Baerends, E. J.; Snijders, J. G. *J. Chem. Phys.* **1996**, *105*, 6505. van Lenthe, E.; van der Avoird, A.; Wormer, P. E. S. *J. Chem. Phys*. **1998**, *108*, 4783.
(17) van Wüllen, C. *J. Chem. Phys.* **1998**, *109*, 392.
(18) Ahlrichs, R.; May, K. *Phys. Chem. Chem. Phys.* **2000**, *2*, 943.
(19) Schäfer, A.; Horn, H.; Ahlrichs, R. *J. Chem. Phys.* **1992**, *97*, 2571.
(20) Schäfer, A.; Huber, C.; Ahlrichs, R. *J. Chem. Phys.* **1994**, *100*, 5829.
(21) Eichkorn, K.; Treutler, O.; Ohm, H.; Haser, M.; Ahlrichs, R. *Chem. Phys. Lett*. **1995**, *240*, 283. Eichkorn, K.; Weigend, F.; Treutler, O.; Ahlrichs, R. *Theor. Chem. Acc*. **1997**, *97*, 119. The Mo atom used an uncontracted basis constructed "by inspection" in the ORCA program.

(22) The SpecialGridIntAcc parameter in ORCA was set to 14, 7, 5, and 5 for the Mo, S, N, and O atoms, respectively.

(23) Neese, F. *J. Chem. Phys.* **2005**, *122*, 034107.

of theory. The reader is referred to refs 24−27 for full details of the above methodology.

The canonical molecular orbitals (MOs) formed from the self-consistent unrestricted Kohn−Sham determinant did not correspond exactly to a spin doublet eigenstate, the α and β frontier orbitals possessing appreciably different spatial and energetic behavior. This made the interpretation of the **g** and **A** matrices obtained from the CP-SCF procedure in terms of an intuitive ligand field (LF) picture very difficult. Spin degeneracy can be achieved by unitary transformation to a single determinant of spin-degenerate natural orbitals[28] or, in this instance, unrestricted natural orbitals (UNOs);[29] however, the UNO energies are not uniquely defined because the matrix of Lagrange multipliers in the Kohn−Sham equations is no longer diagonal. The mapping onto a LF picture was therefore accomplished by analyzing the quasi-restricted molecular orbitals (QRMOs)[5,30] implemented in the ORCA program. Here the SOMO takes on the spatial form of the singly occupied UNO, with its α and β energies determined by the expectation values of the spin-up and spin-down Fock operators applied to the UNO; i.e., the α and β orbitals of the SOMO are restricted to share the same spatial orbital but are assigned distinct energies. One takes the doubly occupied molecular orbitals (DOMOs) to be the essentially doubly occupied UNOs but transformed such that they diagonalize the spin-down Kohn−Sham operator. The virtual space of the QRMO's is spanned by the essentially unoccupied UNOs which are linearly transformed to diagonalize the spin-up Fock operator.[31]

This pragmatic approach can be used to map the spin-polarized canonical orbitals onto an MO diagram and enables a qualitative understanding of the *g* shifts obtained at the BP86 level.[32] For pure functionals, the solution of the CP-SCF problem reduces to a familiar (uncoupled) sum-over-states expression from perturbation theory, which involves cross-terms between the OZ and SOC matrix elements. With labeling of the doubly occupied orbitals by *i*, the singly occupied orbital by *p*, and the virtual molecular orbitals (VMOs) by *a*, the quasi-restricted **g** matrix was computed from[24,30]

$$\Delta g_{\mu\nu}^{\mathrm{OZ/SOC}} = -\frac{1}{S}\sum_i \frac{\langle\psi_i|l_\mu|\psi_p\rangle\langle\psi_p|h_\nu^{SOC}|\psi_i\rangle}{\epsilon_p^{\beta} - \epsilon_i^{\beta}} + \frac{1}{S}\sum_a \frac{\langle\psi_p|l_\mu|\psi_a\rangle\langle\psi_a|h_\nu^{SOC}|\psi_p\rangle}{\epsilon_a^{\alpha} - \epsilon_p^{\alpha}} \quad (4)$$

where $S = 1/2$ and h_ν^{SOC} is the spatial part of the mean-field spin−orbit operator.[23] The first term in eq 4 corresponds to DOMO → SOMO transitions, and the second term, to SOMO → VMO transitions; these utilize the unique β and α SOMO energies, respectively. The principal values and directions (*x*,*y*,*z*) of the physically observable symmetric **g** matrix was then computed from the (square-root of) eigenvalues and eigenvectors of $\mathbf{g}^{\mathrm{T}}\cdot\mathbf{g}$.

Since only minor structural changes are purported to accompany solvation of molybdenyl ene−dithiolate complexes, including Tp*MoO(bdt),[33] we have assumed that the X-ray crystallographic structures are adequate representations of the structures in frozen solution. On the other hand, geometry optimization in the gas phase (isolated molecule) has recently been shown to influence the metal−dithiolate fold angle of Tp*MoO(bdt), where it was found to increase from 21° in the solid state to 31° in the gas phase.[34] Given the substantial difference between the calculated spin Hamiltonian parameters of Tp*MoO(bdt) in this work and experiment,[8] we also decided to run the same calculations using its geometry-optimized structure as obtained by Joshi et al.,[34] enabling the relative importance of the change in metal−dithiolate fold angle and gas-phase geometry optimization to the resultant EPR parameters to be gauged.

Results

Table 1 summarizes the principal *g* and *A* values and their relative orientations, obtained from the calculations for each of the complexes studied. The hyperfine values have been separately tabulated with and without the inclusion of the second order contribution, to gauge the importance of this term for Mo. For comparison, the experimentally determined values for these complexes are also provided. Note the conventions used for the Euler angles, whereby α represents a rotation about the "*z*" axis, β represents a rotation about the (new) "*y*" axis, and γ represents a rotation about the (new) "*z*" axis.

To assess the relative importance of ligand-to-metal charge transfer (LMCT), d−d, and metal-to-ligand charge transfer (MLCT) transitions to the *g* shifts, we present the approximate contributions of the DOMO → SOMO and SOMO → VMO transitions to the net QR **g** matrix in Table 2. The influence of a subset of these transitions is provided in Table 3 and Tables S1−S6 (Supporting Information), which give the Löwdin reduced orbital population of selected MOs and their individual contribution to the net *g* shifts. The spatial distribution of the corresponding quasi-restricted MOs is provided in Figure 3 and Figures S1−S6 (Supporting Information), which were generated using the ORCA interface to gOpenMol.[35] This provides a description enabling us to qualitatively explain the results obtained from the more rigorous CP-SCF results listed in Table 1.

The use of the X-ray crystallographic structures in the calculations leads to a loss of strict mirror symmetry in the *XZ* plane, which is reflected in many of the MOs in Figure 3 and Table 3 and Figures S1−S6 and Tables S1−S6. The geometry-optimized Tp*MoO(bdt) structure yielded C_s symmetric MO's (Figure S7), as expected. The bond orders of

(24) Neese, F. *J. Chem. Phys.* **2001**, *115*, 11080.
(25) Neese, F. *J. Chem. Phys.* **2003**, *118*, 3939.
(26) Baute, D.; Arieli, D.; Neese, F.; Zimmermann, H.; Weckhuysen, B. M.; Goldfarb, D. T. *J. Am. Chem. Soc.* **2004**, *126*, 11733, Supporting Information.
(27) Jensen, F. *Introduction to Computational Chemistry*; John Wiley and Sons: Chichester, U.K., 2002; Chapter 10.5.
(28) McWeeney, R.; Sutcliffe, B. T. *Methods of Molecular Quantum Mechanics*; Academic Press: London, U.K., 1969.
(29) Pulay, P.; Hamilton, T. P. *J. Chem. Phys.* **1988**, *88*, 4926. Bofill, J. M.; Pulay, P. *J. Chem. Phys.* **1989**, *90*, 3637.
(30) Schöneboon, J. C.; Neese, F.; Thiel, W. *J. Am. Chem. Soc.* **2005**, *127*, 5840, Supporting Infomation.
(31) Neese, F. Private communication.
(32) The QRMO approach is suitable for pure functionals. The GGA virtual orbital energies, unlike those from Hartree−Fock and hybrid calculations (whose orbitals "see" *N* instead of *N* − 1 electrons), represent adequate zeroth-order approximations to the excitation energies and are thus suitable for inclusion in eq 4.
(33) Inscore, F. E.; McNaughton, R.; Westcott, B. L.; Helton, M. E.; Jones, R.; Dhawan, I. K.; Enemark, J. H.; Kirk, M. L. *Inorg. Chem.* **1999**, *38*, 1401.
(34) Joshi, H. K.; Cooney, J. J. A.; Inscore, F. E.; Gruhn, N. E.; Lichtenberger, D. L.; Enemark, J. H. *Proc. Nat. Acad. Sci. U.S.A.* **2003**, *100*, 3719.
(35) gOpenMol for Linux, v. 2.32, http://www.csc.fi/gopenmol/, 2003.

Table 1. Anisotropic Spin Hamiltonian Parameters for Mo(V) Model Complexes Determined from DFT Calculations Using BP86 and B3LYP Functionals and Comparison with Experimental Data[a]

complex	calc type	g_{xx}	g_{yy}	g_{zz}	$\langle g\rangle^b$	$A_{x'x'}$	$A_{y'y'}$	$A_{z'z'}$	$\langle A\rangle^b$	α^c	β^c	γ^c
Tp*MoO(cat)	BP86	1.9867	1.9796	1.9402	1.9688	9.2	9.5	40.5	19.8	10	43	44
	BP86+A^{SO}					11.7	11.1	46.8	23.3	1	39	−1
	B3LYP	1.9790	1.9725	1.9276	1.9597	16.1	16.4	50.2	27.6	10	42	34
	B3LYP+A^{SO}					19.7	18.6	57.4	31.9	0	37	−2
	expt[d]	1.9680	1.9660	1.9194	1.9511	27.0	26.0	64.2	39.1	0	36	0
	expt[e]	1.969	1.969	1.920	1.953	34.0	20.0	66.2	40.1	0	0	0
Tp*MoS(cat)	BP86	1.9796	1.9757	1.9042	1.9524	13.3	12.7	42.6	22.9	0	36	10
	BP86+A^{SO}					14.8	16.6	49.6	27.0	2	34	6
	B3LYP	1.9698	1.9651	1.8874	1.9408	20.5	19.6	51.8	30.7	1	36	9
	B3LYP+A^{SO}					25.0	22.6	59.9	35.9	2	34	6
	expt[d]	1.9646	1.9595	1.8970	1.9404	30.0	29.0	67.5	42.2	0	34.5	0
Tp*MoO(bdt)	BP86	2.0161	1.9863	1.9508	1.9844	10.77	10.71	38.2	19.9	3	46	16
	BP86+A^{SO}					12.24	12.18	42.6	22.3	2	44	−1
	B3LYP	2.0115	1.9784	1.9413	1.9771	16.4	15.9	47.2	26.5	0	48	−1
	B3LYP+A^{SO}					18.9	18.1	52.6	29.9	0	46	0
	expt[d]	2.0025	1.9730	1.9360	1.9705	24.0	26.0	60.0	36.7	0	45	0
	expt[f]	2.004	1.972	1.934	1.970	50.0	11.4	49.7	37.0	0	0	0
Tp*MoS(bdt)	BP86	2.0079	1.9858	1.9300	1.9745	12.6	13.9	39.6	22.1	2	38	−2
	BP86+A^{SO}					15.8	14.3	44.6	24.9	2	36	−2
	B3LYP	2.0009	1.9756	1.9163	1.9643	19.1	19.7	48.7	29.2	−2	40	−1
	B3LYP+A^{SO}					22.0	22.5	54.9	33.1	2	38	−4
	expt[d]	1.9975	1.9680	1.9159	1.9607	26.0	26.5	59.2	37.2	0	39	0
Tp*MoO(etp)$_2$	BP86	1.9843	1.9568	1.9324	1.9578	16.9	18.3	46.4	27.2	18	34	15
	BP86+A^{SO}					19.1	21.0	53.2	31.1	18	31	4
	B3LYP	1.9772	1.9483	1.9175	1.9477	22.5	24.1	55.3	33.9	17	33	11
	B3LYP+A^{SO}					25.5	27.7	63.3	38.9	17	30	2
	expt[d]	1.9647	1.9417	1.9073	1.9379	33.0	34.0	74.5	47.2	0	26.5	0
Tp*MoS(etp)$_2$	BP86	1.9852	1.9386	1.8963	1.9400	16.6	19.0	45.9	27.2	3	34	26
	BP86+A^{SO}					19.5	22.5	53.8	32.0	3	29	16
	B3LYP	1.9759	1.9256	1.8751	1.9255	23.3	24.7	54.2	33.8	6	34	20
	B3LYP+A^{SO}					26.3	29.5	63.4	39.8	6	30	11
	expt[d]	1.9558	1.9114	1.8623	1.9098	32.0	34.0	72.0	46.0	0	26	0
Tp*MoS(pp)$_2$	BP86	1.9836	1.9356	1.8912	1.9368	16.1	19.3	46.0	27.2	−5	34	−2
	BP86+A^{SO}					19.0	23.1	54.1	32.1	−4	30	−1
	B3LYP	1.9743	1.9229	1.8696	1.9223	21.6	25.0	54.1	33.6	−7	34	−1
	B3LYP+A^{SO}					25.6	30.1	63.5	39.8	−6	31	−1
	expt[d]	1.9575	1.9111	1.8575	1.9087	33.0	34.0	72.0	45.5	0	25	0

[a] The results for $A = A_F + A^{dip}$ and $A = A_F + A^{dip} + A^{SO}$ have been tabulated separately. [b] $\langle g\rangle = 1/3(g_{xx} + g_{yy} + g_{zz})$; $\langle A\rangle = 1/3(A_{x'x'} + A_{y'y'} + A_{z'z'})$; units for coupling constants $= 10^{-4}$ cm^{-1}. [c] Euler rotations (in deg) are defined as $R(\alpha,\beta,\gamma) = R_z(\gamma)R_y(\beta)R_z(\alpha)$. [d] Reference 4. [e] Reference 7. [f] Reference 8.

Table 2. Contribution to the (Symmetrized) Quasi-Restricted **g** Shift Matrix (in ppm) of Transitions to and from the SOMO, as Calculated in the Molecular Coordinate Frame (Figure 1)

complex	transition	Δg_{XX}	Δg_{YY}	Δg_{ZZ}	Δg_{XZ}	Δg_{YZ}	Δg_{XY}
Tp*MoO(cat)	DOMO → SOMO	10 923	10 234	39 537	−3 014	−1 110	207
	SOMO → VMO	−52 566	−31 183	−72 160	26 828	1 094	277
	net	−41 644	−20 948	−32 623	23 814	−16	484
Tp*MoS(cat)	DOMO → SOMO	18 266	14 640	36 159	−5 501	−890	92
	SOMO → VMO	−80 178	−37 079	−80 808	41 874	2 151	−824
	net	−61 912	−22 439	−44 649	36 373	1 260	−732
Tp*MoO(bdt)	DOMO → SOMO	11 168	15 180	59 637	5 196	−34	71
	SOMO → VMO	−39 839	−29 239	−63 540	27 079	668	−183
	net	−28 671	−14 059	−3 903	32 274	634	−112
Tp*MoS(bdt)	DOMO → SOMO	15 732	22 019	54 671	2 421	167	96
	SOMO → VMO	−51 017	−35 497	−73 463	37 545	579	−411
	net	−35 285	−13 478	−18 792	39 966	746	−315
Tp*MoO(etp)$_2$	DOMO → SOMO	7 231	9 536	30 664	−719	−3 280	−1
	SOMO → VMO	−49 831	−52 112	−84 239	22 829	17 499	4 374
	net	−42 600	−42 575	−53 574	22 110	14 218	4 373
Tp*MoS(etp)$_2$	DOMO → SOMO	12 398	16 735	29 187	−3 500	−4 513	1 701
	SOMO → VMO	−71 954	−73 779	−95 408	41 108	28 219	−7 467
	net	−59 556	−57 044	−66 222	37 609	23 706	5 766
Tp*MoS(pp)$_2$	DOMO → SOMO	11 358	17 185	29 130	−3 391	4 367	−1 270
	SOMO → VMO	−72 182	−78 467	−98 355	42 816	−27 980	−3 822
	net	−60 824	−61 282	−69 226	39 426	−23 613	−5 092

the Mo≡E bond are very similar for the terminal oxo and sulfido group, both being around 2.5 (Table S10), which justifies their representation as a formal triple bond.

Discussion

Functional Dependence of the EPR Parameters. The BP86 functional consistently produces a significant under-

Table 3. Löwdin Reduced Orbital Populations of Selected QRMOs for Tp*MoS(bdt) and Their Contribution to the **g** Matrix via SOC to the SOMO, as Calculated Using Eq 4[a]

ΔE (cm^{-1})	MO	Mo (%)	S1 (%)	S2 (%)	S3 (%)	Δg_{XX}	Δg_{YY}	Δg_{ZZ}	Δg_{XZ}	Δg_{YZ}	Δg_{XY}
38 938	LUMO+8	6.2 (6.0d$_{XY}$)	0.2	2.1	1.5	−155	1	−4 241	971	79	−30
37 650	LUMO+7	23.5 (22.8d$_{XY}$)	0.1	7.8	7.4	−1 300	2	−8 235	4 806	246	−26
36 188	LUMO+6	39.0 (34.4d$_{Z^2}$)	17.0	4.0	4.9	−9	−3 650	−39	25	−389	206
33 534	LUMO+5	11.4 (7.3d$_{XY}$, 3.8d$_{YZ}$)	0.4	3.4	2.9	−552	1	−11 643	−2 706	70	8
33 197	LUMO+4	1.3	0.0	1.6	2.3	−4	−67	−426	−44	−179	−17
31 504	LUMO+3	17.3 (15.4d$_{XY}$)	0.6	4.1	5.5	91	46	−20 944	1 040	570	−122
30 553	LUMO+2	15.4 (9.6d$_{Z^2}$, 2.6d$_{XY}$)	3.9	2.5	0.8	−71	214	−3 437	504	−974	182
15 235	LUMO+1	49.8 (47.4d$_{XZ}$, 1.2d$_{X^2-Y^2}$)	25.1	8.1	6.5	−137	−31 101	−12	44	−664	2 063
13 637	LUMO	51.6 (50.0d$_{YZ}$, 1.0d$_{XY}$)	30.9	2.4	3.9	−47 439	−144	−19 986	31 467	1 738	−2 610
0	SOMO	76.5 (73.6d$_{X^2-Y^2}$, 2.9d$_{XZ}$)	3.9	3.1	3.2						
−6 786	SOMO−1	8.1 (4.7d$_{X^2-Y^2}$, 1.4d$_{Z^2}$, 0.5d$_{XZ}$)	12.5	21.3	21.2	11	822	−2	−3	−43	101
−10 289	SOMO−2	0.0	13.2	24.8	24.7	1 119	1	−566	494	19	27
−14 949	SOMO−3	0.0	0.0	0.0	0.1	−29	2	8	48	9	3
−16 272	SOMO−4	1.6	2.5	3.2	3.5	439	3	2 809	1 113	96	37
−17 768	SOMO−5	5.4 (2.8d$_{YZ}$, 1.3d$_{XY}$)	5.9	8.9	7.8	1 293	356	4 978	2 757	1 332	748
−18 143	SOMO−6	10.8 (7.2d$_{XZ}$, 2.1d$_{X^2-Y^2}$)	23.3	1.1	1.2	116	4 576	604	274	−1 670	−774
−19 004	SOMO−7	4.2 (2.2d$_{XY}$)	11.4	8.5	7.6	125	1	2 422	−600	52	−14
−29 644	SOMO−15	23.1 (20.1d$_{XZ}$)	18.2	5.4	11.7	124	6 773	46	−75	−562	918
−35 031	SOMO−16	6.6 (2.5d$_{YZ}$, 1.6d$_{XY}$)	0.1	16.5	14.1	236	30	5 643	1 207	−446	−84
−45 021	SOMO−25	6.3 (5.5d$_{XY}$)	0.0	1.2	0.3	−6	6	6 705	106	218	1

[a] Here S1 denotes the apical sulfido ligand and S2 and S3 refer to the equatorial S ligands.

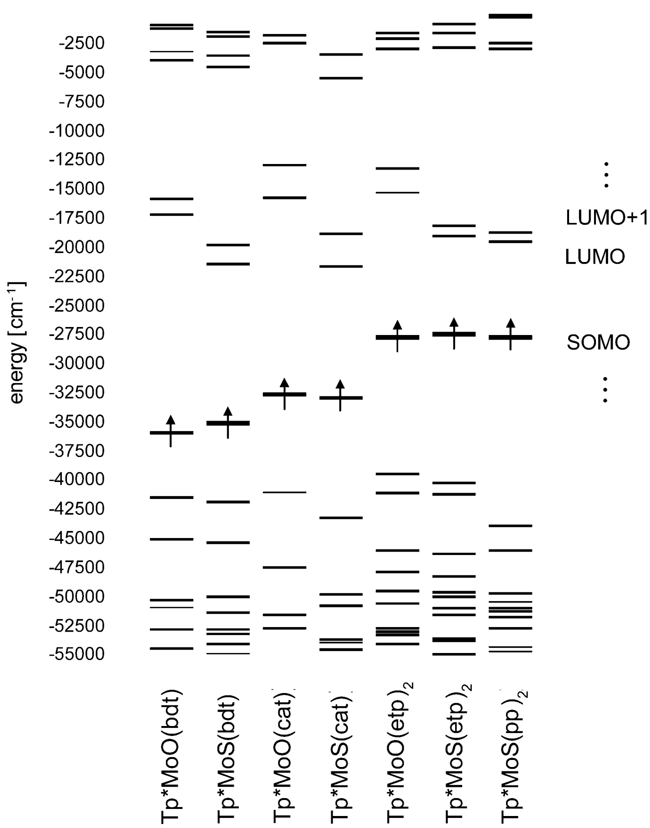

Figure 2. Partial energy level diagram obtained from the QRMO analysis. The unpaired spin denotes the SOMO, whose energy is depicted as the average of the α and β energies. DOMO → SOMO energies are equal to the difference of the respective β orbital energies, and SOMO → VMO energies are equal to the difference of α orbital energies (see text). Refer to Figures 3 and S1−S6 for the spatial representation of the above frontier orbitals; corresponding atomic populations are provided in Tables 3 and S1−S6. Note that ORCA does not output symmetry properties of the orbitals as no symmetry constraints are imposed in the SCF calculations.

estimate of both $A_{\mu\nu}$ and $\Delta g_{\mu\nu}$. The B3LYP calculation yields excellent predictions of the **g** matrix and larger A_{ij} values, although they are still significantly underestimated. These trends highlight the tendency of GGA functionals to overestimate the covalency of polar metal−ligand (M−L) bonds,[11] leading to an underestimated spin density at the metal nucleus using the BP86 functional. Hartree−Fock exchange leads to M−L bonds which are too ionic and hence the augmentation of GGA functionals with some HF exchange tends to compensate for the aforementioned covalency. The hybrid B3LYP functional therefore yields larger metal hyperfine couplings, which, although still underestimated, approach magnitudes much closer to the experimental values.

The overestimated covalency is also responsible for the higher *g* values obtained at the BP86 level. For the SOMO → VMO transitions (d−d and MLCT), a reduced metal character produces smaller negative *g* shifts, while, for the DOMO → SOMO transitions (LMCT), the increased metal character of the ligand orbitals produces larger positive *g* shifts (due to the larger Mo SOC). In both instances, the *g* values are increased.

Basis Set Dependence. To trial any effects due to incomplete basis set and/or a lack of flexibility in the core region, we also tested a fully decontracted well-tempered basis set (WTBS)[36] (which approaches the basis-set limit) for the Mo, while maintaining a decontracted TZVP or SV-(P) for the remaining atoms, as recently used with success by Neese and co-workers.[3] At the BP86 level, the resulting $A_{\mu\nu}$(^{95}Mo) values were found to deviate by less than 1 MHz from those obtained using a decontracted TZVP basis for the Mo atom. Moreover, the principal *g* values differed by only a few parts per thousand in accordance with the less rigorous requirements of DFT on basis set size.

Excitation Energies. Due to the neglect of orbital relaxation associated with excitation processes, the energy differences between the virtual and occupied MOs are only a zeroth-order approximation to the true excitation energies. Nevertheless, given that the VMO energies are used in the

(36) Huzinaga, S.; Miguel, B. *Chem. Phys. Lett.* **1990**, *175*, 289. Huzinaga, S.; Klobukowski, M. *Chem. Phys. Lett.* **1993**, *212*, 260.

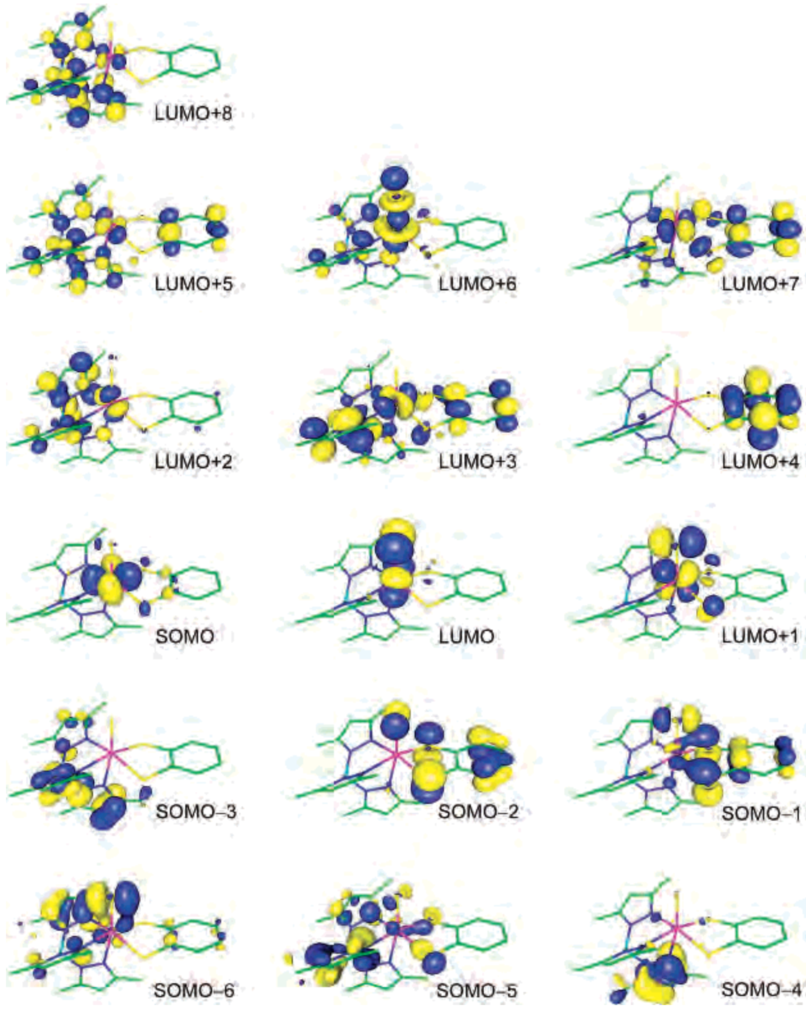

Figure 3. Selected QRMOs obtained for Tp*MoS(bdt). The contours are drawn at 5%. Hydrogen atoms are omitted for clarity.

g matrix calculations, it should still be possible to establish some qualitative trends from the QRMO analysis. Figure 2 shows that the lowest d−d transitions (SOMO → LUMO (lowest unoccupied molecular orbital), LUMO+1) in the sulfido complexes occur at energies some 5000 cm^{-1} lower than the oxo analogues, in agreement with the smaller SOMO−LUMO gap expected for the weaker π-base sulfido ligand compared with the strong π-base oxo ligand;[4] i.e., the LUMO and LUMO+1 are less destabilized due to the weaker interaction with the sulfido ligand. This yields lower g values for the thiomolybdenyl complexes, since the dominant contributions to the **g** matrix arise from admixture of these orbitals into the SOMO (eq 4) upon the application of the static magnetic field.

The sulfido complexes containing monodentate O-donor ligands exhibit a low-energy d−d transition in the near-IR region between 7500 and 7700 cm^{-1} ($\epsilon \sim 100$ M^{-1} cm^{-1}).[4] From Tables S2 and S3 (Supporting Information), the LUMO appears at 8200−8300 cm^{-1} above the SOMO, in reasonable agreement with the near-IR data. With reference to Figure 2, the origin of this low-energy transition is seen to result primarily from a destabilization of the SOMO compared with the complexes containing bidentate donor ligands.

Sulfido complexes containing bidentate benzenoid ligands do not exhibit a band in an accessible region of the near-IR spectrum,[4] in accord with the observation of the lowest d−d transitions of Tp*MoS(bdt) and Tp*MoS(cat) at around 14 000−15 000 cm^{-1} (Table 3) and 11 000−14 000 cm^{-1} (Table S1), respectively. From Figure 2, the smaller SOMO−LUMO gap for the catecholate complex results from a greater destabilization of the SOMO in this instance. The lowest energy near-IR bands in these complexes possess considerable charge-transfer character ($\epsilon > 1800$ M^{-1} cm^{-1}), as do their oxo analogues.[4] Of interest to this work are those LMCT transitions which contribute to the electronic g shifts. A large number of these transitions can be identified; however, these are characterized by a large number of small positive contributions to the net g shifts shown in Table 2 rather than a small number of large contributions. A few of the LMCT donor orbitals are depicted in Figures 3 and S1−S6. Note that the lowest energy LMCTs involving SOMO−1 and SOMO−2 do not provide a significant contribution to the g shifts as seen from Table 3. In particular, the symmetric S_{π}^{+} orbital in SOMO−1 cannot contribute to Δg_{XX} because the contribution from each S atom cancels the other (unlike the shifts from the S_{π}^{-} sulfurs in SOMO−2, which reinforce).

Electron Zeeman Matrices. As g shifts are caused by SOC to excited states involving electron density on the same centers as the SOMO, we need only consider the Mo atom and its first coordination sphere, as can be gauged from the orbital composition of the SOMO in each complex, which typically involves 70−80% Mo character, 3−6% oxygen/sulfur p character, and up to 4% terminal oxo/sulfido character. The Tp* contributions are negligible due to the small atomic percentage and minimal SOC of the nitrogen ligands. With examination of the orbital composition of the $d_{X^2-Y^2}$-based SOMO in each complex, it is evident that the magnetic orbital has typically 2−4% admixture of d_{XZ} and no configurational mixing of d_{Z^2}, as expected on the basis of simple crystal field arguments in our earlier EPR study.[4]

In crystal-field theory and ideal $C_s^{(XZ)}$ symmetry, the principal g_{xx} and g_{zz} directions are predicted to be perpendicular to the d_{YZ} and d_{XY}-based (A″) orbitals, respectively. In molecular orbital theory these orbitals may interact very differently with the ligands and the simple correspondence between LUMO and LUMO+1 orientation and principal g_{xx} and g_{zz} directions no longer holds. The principal g directions are instead determined by the cumulative g shifts arising from a potentially large number of LMCTs, d−d transitions, and MLCTs.

Figures 3 and S1−S6 show that the d_{XY}-based and d_{Z^2}-based MOs involve substantial delocalization onto the Tp* and X donor ligands and there exist a number of closely spaced MOs above the SOMO which could be labeled MLCT states rather than d−d (ligand-field) states. This may arise partly from the tendency of GGA functionals to overestimate covalency (vide supra); however, it is not surprising that the simple crystal-field model used as a guide to interpreting the SH parameters in our previous experimental study is inadequate,[4] since it is known that when large covalency is involved, the contribution of SOC to the HFC predicted by ligand-field theory becomes inaccurate.[25]

With reference to the bidentate complexes in Tables 3, S1, S4, and S5, the SOMO → LUMO ("$\Psi_{X^2-Y^2} \rightarrow \Psi_{YZ}$") transition provides the dominant contribution to Δg_{XZ} and therefore accounts for the bulk of the rotation of the **g** matrix in the *XZ* plane, even with only a relatively modest admixture of d_{XY} in the LUMO. Transitions from the SOMO to d_{XY}-based orbitals also contribute to Δg_{XZ}; however, they do so only modestly due to their larger energy separation and greater delocalization (vide supra). Moreover, the sign of the contribution varies, with a positive Δg_{XZ} being associated with a clockwise rotation of **g** about the *Y* axis and vice versa.

Turning now to the LMCTs, the DOMO → SOMO transitions affect mostly Δg_{ZZ} and are largest for the dithiolate complexes. Moreover, the LMCTs make a positive contribution to Δg_{XZ} for the dithiolate complexes and a negative contribution for all other complexes. The LMCTs clearly provide a substantial augmentation to the g shifts. However, it is difficult to isolate dominant donor orbitals because there is a cumulative effect over a large number of small shifts. From a detailed inspection of the QRMO analysis, it is interesting to note that it is generally the small Mo d_{XY} character of the donor orbitals, which couples to the Mo $d_{X^2-Y^2}$ character of the acceptor orbital, that is of importance to the g shifts rather than the SOC of the ligating atoms themselves. The secondary importance of the ligand SOC, compared with the metal SOC, can be ascertained from SOMO−2 (S_π^-) of Tp*MoS(bdt) (Table 3), which has 50% sulfur character and yet only contributes Δg_{XX} shifts of the order 0.001 because of the small sulfur character in the SOMO. Nevertheless, the LMCT contributions are significantly larger for the bdt complexes compared with the cat complexes, which appears to be due to the closer energy matching of the LMCT donor orbitals and increased covalency of the Mo−S bonds.

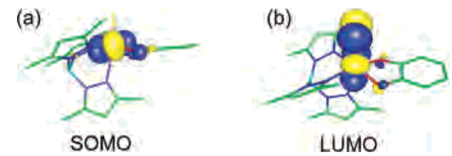

Figure 4. (a) Ground-state magnetic orbital of Tp*MoS(cat) as viewed along the molecular *Y* axis. Admixture of d_{XZ} character into the predominantly $d_{X^2-Y^2}$-based SOMO leads to a rotation of the lobes in the *XZ* plane. The largest principal hyperfine coupling is directed approximately perpendicular to the plane of the SOMO. (b) LUMO as viewed in the *YZ* plane. The rotation of the **g** matrix is in part due to the rotation of the d_{YZ}-based LUMO in the *XZ* plane, which arises from an admixture of d_{XY} character.

All monodentate complexes possess a very similar β Euler angle (Table 1), as observed experimentally, and this can be related to the similar orientations of the etp and pp ligands.[4] It is seen that the two Tp*MoE(etp)$_2$ (E = O, S) complexes possess very similar bond and torsion angles, while Tp*MoS(pp)$_2$ possesses angles almost opposite in magnitude and sign to Tp*MoS(etp)$_2$. In fact, if we ignore the phenolate side chains, Tp*MoS(etp)$_2$ and Tp*MoS(pp)$_2$ are roughly mirror images of each other (cf. Figures 1 and 3 of ref 4). The consequences of this are evident from a comparison of their α and γ Euler angles in Table 1, which have their magnitude and sign interchanged for these two complexes, and from Table 2, where Δg_{YZ} and Δg_{XY} have opposite magnitude and sign. The nonzero α and γ Euler angles can easily be associated with the rotation of the LUMO and LUMO+1 orbitals away from the *YZ* and *XZ* planes, respectively, and the approximate mirror symmetry of the X = etp and X = pp complexes leads to the approximate mirror symmetry of the MOs in each system (compare Figures S2 and S3).

Nuclear Hyperfine Matrices. Unlike the **g** matrix, which depends on the energy and composition of a large number of MOs, the principal hyperfine directions are much simpler to interpret since the **A** matrix is determined primarily by the SOMO.[4] We may therefore expect $A_{z'z'}$ to be oriented perpendicular to the plane of the SOMO and the admixture of d_{XZ} into the SOMO means that it is rotated slightly away from the Mo≡E (E = O, S) bond direction (Figure 4). Thus, for the (ideally) C_s-symmetric cat and bdt complexes, there should exist a correlation between the degree of d_{XZ} admixture with the noncoincidence angle between $A_{z'z'}$ and the molecular *Z* axis ($\angle z'Z$). Table 4 shows that this trend is indeed followed (the small variation between the much larger $d_{X^2-Y^2}$ percentage character is negligible for the purposes of this qualitative comparison). Similar behavior applies to the triclinic monodentate complexes, except additional admixture of d_{YZ} further rotates the plane of the SOMO.

Table 4. Orientation of g_{zz} and $A_{z'z'}$ from the Molecular Z Axis (Mo≡O,S Bond Direction) and the Euler Rotation (β) from **A** to **g**[a]

complex	∠zZ (deg)	∠$z'Z$ (deg)	β (deg)	∠zZ (QRMO) (deg)	d_{XZ} (QRMO) (%)	fold angle (deg)
Tp*MoO(cat)	47	10	37	50	2.0	18.3
Tp*MoS(cat)	50	16	34	51	4.1	21.1
Tp*MoO(bdt)	54	9	46	55	1.8	21.3
Tp*MoS(bdt)	50	13	38	50	2.9	25.3

[a] Angles are taken from CP-SCF calculations at the B3LYP level, including second order contributions to the **A** matrix. For comparison, we also provide the orientation of the **g** matrix as calculated from the QRMO analysis. The percentage of d_{XZ} character in the SOMO is also tabulated and can be correlated with the rotation of the **A** matrix (∠$z'Z$).

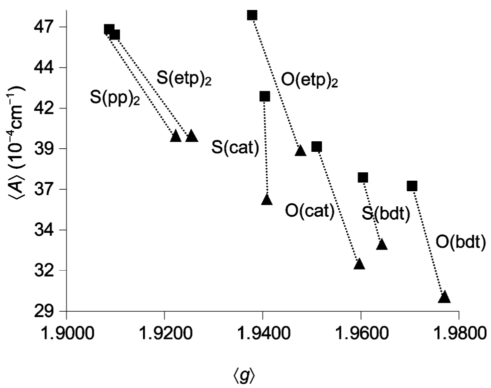

Figure 5. Inverse correlation of ⟨g⟩ and ⟨A⟩(^{95}Mo) for the complexes listed in Table 1 and their comparison with the experimental data of ref 4. Points are labeled with the EX_2 portion from the corresponding formula Tp*MoEX_2. The squares and triangles are the experimental and theoretical data points, respectively. The dotted lines simply connect the theoretical and experimental data points for the same compound.

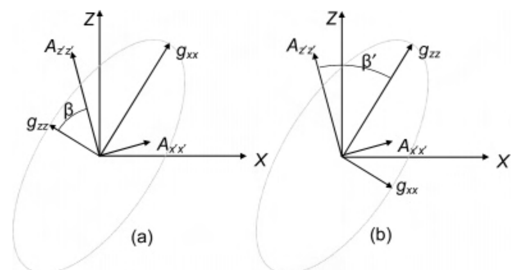

Figure 6. Schematic representation of the relative orientation of the principal **g** and **A** directions in C_s symmetry as viewed along the molecular Y axis. Here the principal axes of **g** are (x, y, z), and those of **A** are (x', y', z'). Depending on whether one chooses to assign (a) $g_{xx} = g_{max}$ and $g_{zz} = g_{min}$ or (b) $g_{zz} = g_{max}$ and $g_{xx} = g_{min}$, the magnitude of the Euler rotation connecting the **g** and **A** coordinate systems is either (a) β or (b) $\beta' = 90 - \beta$.

Note that the magnitude of the dipolar HFC is very similar for all complexes and levels of calculation, the major differences arising from ⟨A⟩ (Table 1). The inclusion of SOC contributions to the **A** matrix is significant, and the pseudocontact interaction increases the isotropic hyperfine couplings by ca. 10−20%. In addition, the second-order dipolar component of A^{SO} generally rotates **A** away from the Z axis by an additional 2−5° and therefore reduces β by 2−5° (Table 1).

In contrast to the dipolar component, whose directional behavior can be correlated with the configurational mixing in the SOMO, it is not possible to correlate the percentage Mo character of the SOMO with the magnitude of ⟨A⟩. This is because the QRMO analysis cannot account for the core polarization at the nucleus, which results naturally from the spin-polarized unrestricted Kohn−Sham approach.

Correlation of ⟨g⟩ and ⟨A⟩. Figure 5 plots the theoretical ⟨g⟩ and ⟨A⟩ listed in Table 1 (B3LYP functional and inclusion of A^{SO}) and compares them with those obtained experimentally.[4] A similar inverse correlation is followed, whereby the presence of sulfur donor atoms cis to the Mo≡S bond results in a larger ⟨g⟩ being associated with a smaller value of ⟨A⟩, whereas oxygen donors give rise to smaller values of ⟨g⟩ associated with larger ⟨A⟩ (compare Tp*MoE(bdt) with Tp*MoE(cat), E = O, S). Also in accord with experiment, the thiomolybdenyl complexes have reduced ⟨g⟩ compared with their molybdenyl analogues.

Inspection of Table 1 shows that both ⟨Δg⟩ = g_e − ⟨g⟩ and ⟨A⟩ are underestimated using the unrestricted Kohn-Sham CP-SCF approach with the hybrid B3LYP functional by around 15%, on average, as reflected by the overpredicted ⟨g⟩ and underpredicted ⟨A⟩ in Figure 5.

Noncoincidence Angles. The noncoincidence of the **g** and **A** ellipsoids is specified by introducing up to three Euler angles describing a set of rotations needed to bring the principal **A** axes into alignment with those of **g**. However, there exists a degree of arbitrariness, since there are 36 distinct ways of permuting each of the three principal g and A values and hence a commensurate number of ways of assigning the Euler angles; these are all mathematically equivalent and lead to the same spin Hamiltonian. In our previous experimental EPR study,[4] we assigned $g_{zz} = g_{min}$ and $g_{xx} = g_{max}$, in addition to assigning $A_{z'z'} = A_{max}$. The motivation for this was based upon the heuristic assignment $A_{z'z'}$↔ "$A_{||}$", g_{zz} ↔ "$g_{||}$", $A_{x'x'} \approx A_{y'y'}$ ↔ "$A_{\perp}$", and g_{xx}, g_{yy} ↔ "$g_{\perp}$". With the aid of the present calculations we can see that although the **g** matrix is rotated by a large angle in the molecular XZ plane, both the largest g value and the largest A value still lie closest to the Mo≡E bond direction (Figure 6). With the exception of Tp*MoO(bdt), all complexes yielded β Euler angles <45°. While it is possible to reorder the assignment of the principal axes to also make β < 45° in this instance, doing so does not add any extra physical significance, and using a different convention for this complex alone would only hinder comparison with the rest of the series.

The origin of the spin Hamiltonian parameters fitted to the randomly oriented EPR spectra[4] now becomes clear. For the nominally monoclinic complexes, we show in Table 4 the orientations of the principal axes of both **g** and **A** matrices with respect to the molecular coordinate frame, as well as their relative orientation. Note that this relative orientation will be highly dependent upon an accurate calculation of the orientational dependence of both interactions. As noted

Table 5. Anisotropic Spin Hamiltonian Parameters for Tp*MoO(bdt) Obtained at the B3LYP Level Including Second-Order Hyperfine Contributions (A^{SO}), Using Both the X-ray Crystallographic and Gas-Phase Geometry Optimized Structures, Together with Experimental EPR Data[a]

method	g_{xx}	g_{yy}	g_{zz}	$\langle g \rangle^b$	$A_{x'x'}$	$A_{y'y'}$	$A_{z'z'}$	$\langle A \rangle^b$	α^c	β^c	γ^c	fold angle (deg)
DFT(cryst)	2.0161	1.9863	1.9508	1.9844	18.9	18.1	52.6	29.9	0	46	0	21.3
DFT(opt)[d]	2.0189	1.9691	1.9242	1.9707	18.0	20.2	52.5	30.3	−1	36	1	31.0
expt[e]	2.0025	1.9730	1.9360	1.9705	24.0	26.0	60.0	36.7	0	45	0	

[a] The metal−dithiolate fold angle is included for comparison. [b] $\langle g \rangle = 1/3(g_{xx} + g_{yy} + g_{zz})$; $\langle A \rangle = 1/3(A_{x'x'} + A_{y'y'} + A_{z'z'})$; units for coupling constants = 10^{-4} cm^{-1} [c] Euler rotations (in deg) are defined as $R(\alpha,\beta,\gamma)=R_z(\gamma)R_y(\beta)R_z(\alpha)$. [d] Structure taken from ref 34. [e] Reference 4.

above, inclusion of the second-order contributions to the hyperfine interaction rotates **A** by an additional 2−5° and is therefore important.

It is worth reiterating that the crystallographic structures used in the computations do exhibit a degree of "buckling" of the Tp* and cat/bdt ligands, especially for Tp*MoO(cat), leading to a deviation from ideal C_s symmetry. This appears to result in a substantial γ Euler angle in the DFT calculations (Table 1). However, $A_{x'x'}$ and $A_{y'y'}$ are close in magnitude; hence, the influence of the final rotation γ on the net **A** matrix is minimal and leads to imperceptible differences in the EPR spectra, which are unlikely to be accurately simulated due to limited experimental resolution.[4] This is particularly evident for the BP86 calculations, which yield $A_{x'x'}$ and $A_{y'y'}$ values that differ by less than 0.5×10^{-4} cm^{-1} in some instances (Table 1), together with large values of γ. The hybrid calculations, on the other hand, appear less sensitive to this, presumably as a consequence of the reduced covalency of the metal−ligand bonds.

Relationship between Euler Rotation and Metal−Dithiolate Fold Angle. We repeated the DFT analysis using the geometry-optimized structure of Tp*MoO(bdt) obtained by Joshi et al.,[34] where the methyl groups of the Tp* ligand were replaced by hydrogen atoms for simplicity. The DFT-calculated spin Hamiltonian parameters and a comparison with those obtained using the crystallographic structure of Dhawan and Enemark[8] are given in Table 5. Additional data summarizing the results from the quasi-restricted molecular orbital (QRMO) analysis are provided in Tables S7−S9 and Figures S7 and S8.

The results show that the $d_{X^2-Y^2}$ character of the SOMO decreases from 73% to 66% and the d_{XZ} character increases from 1.8% to 2.4% upon optimizing the geometric structure. Thus, the folded complex is more covalent than the unfolded complex. The agreement between the experimental and calculated (gas-phase-optimized geometry) principal g values was much better. Although the QRMO data suggest the Mo character of the SOMO is reduced, the principal hyperfine couplings are virtually unchanged (Table S4). This is because the QRMO analysis cannot account for the core polarization at the nucleus, which requires the spin-polarized unrestricted canonical orbitals.

The increase in fold angle by 10° produces a change in the orientation of the principal g axes of the same magnitude, which suggests a possible correlation between metal−dithiolate fold angle and the orientation of the **g** matrix. However, variations of the entire molecular structure accompany the geometry optimization and a systematic study of the EPR parameters as a function of changing fold angle remains to be carried out. It is interesting to note that using the crystallographic structure yields an Euler angle more in line with the 45° obtained from simulation of the frozen-solution EPR spectra (Table 5).

Relevance to Molybdenum Enzymes. Of particular interest to molybdenum enzymes are the complexes with dithiolate donor ligands. It has been shown that Mo(V)−dithiolene complexes may exhibit a very low energy barrier (<1 kcal mol^{-1}) to changing fold angle over a range of more than 30°,[37] with the precise fold angle adopted being dependent upon the nature of surrounding counterions. Moreover, metal−dithiolene covalency of the SOMO was observed to be sensitive to fold angle, with unfolded complexes exhibiting less covalency than folded complexes. The metal−dithiolate fold angles have therefore been implicated as a key factor in the ability of the pterin ring to fine-tune the electron density at the active site of molybdenum enzymes.[34,38] The Mo−di(thi)olate fold angles for the bidentate complexes are given in Table 4, where they are contrasted with the rotation of the **g** matrix about the Y axis, as calculated by the CP-SCF equations at the B3LYP level, as well as by the QRMO method at the BP86 level. From Table 4, no clear relationship can be established between the fold angle and the rotation of **g** and **A**, due to the differences in apical and equatorial ligands in each instance. However, a comparison of the theoretical spin Hamiltonian parameters for Tp*MoO(bdt) using both the X-ray crystallographic structure and the gas-phase geometry-optimized structure shows a difference in fold angle of around 10° leads to a change in β of the same magnitude. It would be worthwhile to pursue this further using the present theoretical approach, to examine the correspondence over a wide range of different fold angles (while maintaining the remaining molecular structure fixed). Such investigations, currently underway, would be of direct interest to EPR spectroscopic studies of Mo enzymes containing one or two pterin ene−dithiolate ligands and could possibly be used as a potential indicator of dithiolate fold angle and pterin oxidation state in the absence of X-ray crystal structures for the Mo(V) state.

Conclusions

The SH parameters for the Tp*MoEX$_2$ series of complexes have been calculated using the CP-SCF formalism at the all-electron level, including scalar relativistic effects and an accurate mean-field SOC operator. The origin of the principal orientations of the electron Zeeman and ^{95}Mo nuclear hyperfine interactions was established, and the electronic

(37) Domercq, B.; Coulon, C.; Fourmigué, M. *Inorg. Chem.* **2001**, *40*, 371.
(38) Joshi, H. K.; Enemark, J. H. *J. Am. Chem. Soc.* **2004**, *126*, 11784.

structure was investigated using a quasi-restricted MO approach unique to the ORCA program.

The inclusion of second-order contributions to the hyperfine coupling (pseudocontact and second-dipolar interactions) is seen to be non-negligible for heavier nuclei such as Mo. For GGA functionals, the underestimated hyperfine couplings can be traced back to an underestimated Fermi contact interaction, which results from an overestimated bond covalency. Likewise, the *g* values are consistently overestimated due to larger metal−ligand covalency. The situation is seen to be dramatically improved by the inclusion of a nominal amount of HF exchange (which by itself leads to bonds which are too ionic) in the hybrid functional. Aside from arbitrarily increasing the level of HF exchange further, improved estimates of the **g** and **A** matrices probably await the arrival of better density functionals.

The present calculations show that the impact of LMCTs to the **g** matrix is dominated by the large Mo SOC rather than the O and S ligand SOC. Thus, the degree of covalency and, hence, the percentage Mo character modulate the contribution of LMCTs to the *g* shifts. The largest such contributions are to Δg_{ZZ}, which arises from the SOC of the Mo d_{XY} character (typically a few percent) of the ligand-based orbital to the Mo $d_{X^2-Y^2}$ character of the SOMO.

The B3LYP calculations yielded both the best electronic Zeeman and nuclear hyperfine data, their agreement with our previous simulations of the experimental EPR spectra of the thiomolybdenyl complexes being remarkably good.[4] The less satisfactory agreement of the DFT with the experimental EPR data for the Tp*MoO(cat) and Tp*MoO(bdt) complexes taken from the literature,[7,8] on the other hand, suggests an unsatisfactory simulation of the frozen-solution X-band EPR spectra in these instances. While the agreement between the experimental and theoretical principal *g* values was quite good in the above cases, DFT predicts a large noncoincidence angle between g_{zz} and $A_{z'z'}$, whereas only an orthorhombic SH was given for these complexes. Moreover, the DFT shows that there exists only a small “in-plane” anisotropy of the **A** matrix ($A_{x'x'} \sim A_{y'y'}$), which is also in contrast to the previously published data.[7,8] Our multifrequency EPR study[4] of these two complexes showed that they had monoclinic C_s symmetry and that the **g** and **A** matrices and large β Euler angles obtained through computer simulation studies are found to be in agreement with those predicted from the DFT calculations (Table 1).

The use of a gas-phase geometry-optimized structure for Tp*MoO(bdt) had little effect on the Mo HFC but did lead to an improvement in the principal *g* values with experiment, with a change in the **g** orientation and, hence, β, commensurate with the change in metal−dithiolate fold angle. Notwithstanding, we still find that $\beta \gg 0$ for either geometry, which disagrees with previous experimental data for this complex. A more systematic study of the effect of varying fold angle on the **g** matrix is required to further establish the nature of this relationship over a broad range of angles and is currently being undertaken. It would also be useful to examine the inclusion of relativistic effects at the all-electron level, together with solvation effects[39] on the geometry optimizations.

Acknowledgment. We thank Dr. Frank Neese, Max-Planck-Institut für Bioanorganische Chemie, Mülheim, Germany, for providing the ORCA program and for helpful discussions. This research was funded by the Australian Research Council.

Supporting Information Available: Selected molecular orbitals (Figures S1−S7) and Löwdin reduced orbital populations (Tables S1−S7) of Tp*MoS(cat), Tp*MoS(etp)$_2$, Tp*MoS(pp)$_2$, Tp*MoO(bdt), Tp*MoO(cat), Tp*MoO(etp)$_2$, and geometry-optimized Tp*MoO(bdt), DFT-calculated EPR parameters (Tables S8 and S9) and partial energy level diagram (Figure S8) for geometry-optimized Tp*MoO(bdt), listings of Löwdin bond orders (Table S10), positional coordinates for the disordered Tp*MoO(etp)$_2$ (Table S11), Tp*MoS(pp)$_2$ (Table S12), Tp*MoS(bdt) (Table S13), and Tp*MoS(etp)$_2$ (Table S14) complexes and for Tp*MoS(cat) (Table S15) and Tp*MoO(cat) (Table S16). This material is available free of charge via the Internet at http://pubs.acs.org.

IC060586B

(39) Klamt, A.; Schüürmann, G. *J. Chem. Soc., Perkin Trans. 2* **1993**, 799.